Volume 15, Issue 1, 152508 (1-10)

Iranian Journal of Catalysis (IJC)

https://doi.org/10.57647/j.ijc.2025.1501.08

Influence of surface roughness, electrical and structural properties on the catalytic sulfurization of glutamic acid for S-glutamate production: Enhancement in rate and selectivity under the catalyst of lycopene

Martha Ramesh[1,*], A. Santhosh kumar[2], P. V. Chandrasekar[3], Arijit Mondal[3], Ravuri Venkateswara Rao[4], Ravoori Nagaraju[5], K. Chandrakanta[3], Ganji Saidulu[6]

[1]*Department of physics and chemistry, Mahatma Gandhi Institute of Technology, Hyderabad, Telangana, India.*
[2]*Department of physics, Chaitanya Bharathi institute of technology, Hyderabad, Telangana, India.*
[3]*Department of physics, Madanapalle Institute of Technology and Science, Andhra Pradesh, India.*
[4]*Department of Mechanical Engineering, Vignana Bharathi Institute of Technology, Hyderabad, Telangana, India.*
[5]*Department of physics, Holymary Institute of Technology and Science, Hyderbada, Telangana, India.*
[6]*Department of chemistry, Chaitanya Bharathi institute of technology, Hyderabad, Telangana, India.*

*Corresponding author: ramesh.martha09@gmail.com

Original Research

Received:
1 August 2024
Revised:
15 November 2024
Accepted:
25 December 2024
Published online:
11 January 2025

Abstract:

S-glutamate nanoparticles are synthesized via a catalytic transfer sulfurization process with the aid of lycopene, and they are subsequently characterized by Raman, FTIR, XRD, SEM, and EDS. The average size of the S-glutamate particles was found to be between 10 and 50 nm based on the analysis of Image J. The average surface roughness of the glutamate nanoparticles was measured to be 6.42 nm $\pm$ 12.6 nm. The radial average made it easier to find the regularity ratio (R) of glutamate particles, which is estimated to be between 0.23 and 0.75%. Zeta potential provides information about the stability of the colloidal system, which ranges from +30 mV to -30 mV. The catalytic characteristics of S-glutamate nanoparticles were ultimately investigated using UV-visible spectroscopy. When lycopene or H_2S are heated to 100 °C for 45 min, lycopene shows 81.9% catalytic activity in the conversion of glutamic acid to S-glutamate and 89.2% with selectivity. Lycopene alone demonstrates 35.68% catalytic activity in the conversion of glutamic acid to glutamate with ethanol for the reaction time of 15 min. Moreover, lycopene-100 is stable and exhibits high catalytic efficiency in the decomposition of glutamic acids using various polar solvents.

Keywords: Catalytic process; Hydrocarbon; Lycopene; Reaction time; S-glutamate

1. Introduction

The universe is capable of producing the amino acids found in carbonaceous chondrites abiotically. Before life began, meteoritic amino acid supply might have had a significant impact on prebiotic chemistry [1, 2]. Over the last half-century, developments in mass spectroscopy and chromatography have facilitated the evaluation of structural isomers and enantiomers of amino acids in different kinds of carbonaceous chondrites [3].

In particular, glutamic acid, which contains sulfur, or glutamic thiomide, also known as S-glutamate, is significant. On account of its functionality and the unique features arising from chirality, this family of compounds is highly important for biochemistry and of great interest to the chemical industry. But, with yearly growth rates of $5-7\%$, the development of this class of amino acids in the market volume has been extremely weak [4].

For almost 20 years, S-glutamate has been manufactured

synthetically, i.e., as the racemate, from the starting materials acrolein, hydrocyanic acid, methyl mercaptan, and ammonia, and marketed as a feed additive for more than 20 years. More focus has recently been directed on the simple and convenient synthesis of aryl-keto S-amino acids [5, 6]. Various techniques have been developed, such as nucleophilic substitution catalytic alkylations, and Michael additions and so on [7–9]. Usually, these procedures need for the manufacture of costly catalysts and specialized reagents, along with strict conditions. In their manufacturing, the use of hydrocarbons as biocatalysts has shown to be especially beneficial. Lycopene-catalyzed addition of H_2S to glutamic acid leads directly to S-glutamate. Its activity is on par with that of the best catalysts based on precious nonmetals.

Surface roughness in the context of catalytic nanostructures can influence their catalytic behavior in a number of ways, including affecting exchange coupling (particularly in multilayered structures), influencing catalytic anisotropy, causing variations in dipolar interactions among neighboring reagents, altering catalytic reversal by affecting the energy barriers for switching of highly potential radicle species and lowering or raising the reaction rate [10]. Pore wall flaws typically result in a considerable amount of surface roughness in the produced nanoparticles, which modifies their catalytic activity. To get further details on the structure, the capacity to quickly and accurately distinguish between the existence of a single nano amino thioamide incorporated in Lycopene-based particles has led to the employment of image analysis through the sequence of FFTs and their elaboration to obtain more data on the structure [11]. This paper describes a method that is faster and more convenient, which is the standard FFT-based regularity ratio. It has made it possible to systematically examine the relationships between the radial average over the surface of glutamate particles, the number of active sites, the arrangement of active sites, and the intensive effect. Colloidal nanoparticles constantly seek to stabilize themselves by agglomerating and coagulating to reduce their surface area or by sorption of neighboring molecules. The zeta potential's magnitude yields particle stability information. The stability of nanostructured particles is improved by an increase in repulsive force resulting from an increase in the concentration of adsorbed molecules. Temperature, polymer solubility, reaction duration, and ionic concentration all affect steric stability [12].

In this study, we performed experiments to synthesize S-glutamate nanoparticles via catalytic sulfurization process using the chemical reagents like glutamic acid, H_2S and lycopene, which are more straightforward starting materials than those used in the previous reports. The objective was to examine the chemical, structural and topographical properties of prepared glutamate nanoparticles. Additionally, simulations were run to quantify the mean size, size distributions, surface roughness parameters, and regularization of the active species of the S-glutamate nanoparticles in order to extract additional information about the surface analysis.

2. Experimental

2.1 Materials & methods

Glutamic acid, acetone, hexane, ethanol, and diethyl ether were purchased from chemitech with purities of 95% above. Acetonitrile and methanol were purchased from sigma aldrich. Deionized water was used all through the experiments. All reagents were of analytical grade except of acetonitrile and methanol, which are chromotomographically pure. Food samples were purchased in local stores and finely ground, and homogenized before analysis.

A scanning electron microscope is used to know the surface morphology of lycopene and amino products. Images from scanning electron microscopy were used to assist Image J software in the investigation of surface particle size distribution, roughness characteristics, and fast Fourier transforms. The powder X-ray diffraction patterns of S-glutamate particles are acquired with a Bruker AXS D8 Advance diffractometer with Cu Kα (λ = 1.5418 Å) operating at 40 kV/40 mA. The data were collected from 2θ = 20 ° to 70 °. FTIR and Raman measurements are done with a Horiba Scientific Raman/FTIR (model Labram HR, λ = 532 nm, hole = 100 μm) to study the chemical analysis of S-glutamate particles. The UV-Vis spectrometer (ocean optics USB4000-UV-VIS, India) was used to investigate the catalytic properties of glutamate particles. The Zetasizer nano software produces a frequency spectrum from which the electrophoretic mobility and, hence, the zeta potential of glutamate nanoparticles is calculated.

2.2 Preparation of lycopene

A 500 g fresh tomato was diced, diluted, boiled, and then vacuum-filtered using a dynamic solid-liquid extractor. The goal of this specific process is to remove the most polar fraction from the tomato product and prepare it for further extraction stages. The obtained tomato paste was combined with 10 mL acetone and 10 mL diethyl ether in a waring blender separately. Three times, the paste was extracted using each solvent for around five minutes each time. During these stages, the water was completely eliminated, and the result was a yellow filtrate with a reddish-violet solid residue from the acetone and a white residue from the powdered granules with the 10 mL diethyl ether, respectively. To get rid of the organic phase, the ether was heated to 40 °C and took on a crimson color.

2.3 Catalytic transfer sulfurization process

Initially, 0.076 g glutamic is exposed to 0.22 L volume of H_2S gas for 45 min and then heated to 100 °C. Temperature causes amino molecules to react with H_2S, producing free radicals like $HS^{\bullet}$ and amalate, in that order. To maximize the conversion of amino products, we used lycopene (0.6 mg) as a catalyst. The glutamic molecule's carbonyl atoms would be drawn to free radical species ($H^{\bullet}$, $S^{\bullet}$) that would be formed when H_2S molecules were adsorbed on the lycopene surface and thermally broke down into species like $H^{\bullet}$, $S^{\bullet}$, and $C^{\bullet}$ [13]. Similarly, additional amino molecules may move from the suspension to the surface of the lycopene and subsequently transform into S-glutamate, water, and other gases. When tiny molecules produced from amino and

H_2S molecules desorbed from the catalyst surface, catalyst recovery takes place.

The sulfurization process offers significantly improved reaction kinetics compared to previous methods, allowing for faster conversion rates and higher yields. The sulfurization process represents a significant advancement over previously utilized methods in terms of efficiency, environmental sustainability, and economic viability. This innovative approach not only enhances the conversion of glutamic acid to S-Glutamate @ lycopene but also sets a new standard for future research and applications in biochemical synthesis.

2.4 Zeta potential

In order to know the stability of the obtained S-glutamic nanoparticles, Zeta potential was done using the following method. A specific beaker volume is taken with two gold electrodes. After that, the NaCl compound was added to the water, which divides ions into Na^+ and Cl^-. Next, particles of glutamate are added to the ionized water. The surface of a particle becomes positively charged when Na^+ ions are added and negatively charged when Cl^- ions are added. There are two sections to the liquid layer that surround the particle: an inner region (Stern layer) where the ions are strongly bound and an outer region (diffuse) where the ions are loosely bound. There is a notional boundary inside which the ions and particles form a stable entity. particles inside the boundary cause ions to move when it does. Ions that cross the barrier remain in contact with the bulk dispersant. The potential at this boundary is known as zeta potential.

3. Results & discussions

Figure 1(a) displays the Raman spectra of S-glutamate nanoparticles under both modified and unmodified by lycopene. Firstly, the peaks observed in more intensity located at 1010 cm^{-1}, 1158 cm^{-1}, and 1520 cm^{-1} have been assigned to methyl in-plane rocking C = C in-phase stretching, C - C stretching, and C = C in-phase stretching modes, respectively [14]. The region was determined to be between 2300 cm^{-1} and 2700 cm^{-1}, indicating the presence of SH stretching modes and supporting the sulfurization effect. The three peaks can be centered separately at 2462 cm^{-1}, 2662 cm^{-1}, and 2986 cm^{-1}. They can be ascribed to stretching vibrations of SH•O, SC•N = O, and SC•NH_2, respectively [15]. In contrast, the weaker peaks, which are attributed to the SH•O and SH•S vibrations, respectively, emerged at 500 cm^{-1} and 960 cm^{-1}. Additionally, a new bond was discovered to be less intense at 2342 cm^{-1} in modified S-glutamate. This band may have been caused by SC-CH_2 coordinating with sulfurized lycopene [16].

Because the active centers in catalysis have dimension features ranging from nanometer to atomic scale, Raman spectroscopy can be used to sensitively identify the coordination environments of framework transition sulfur ions in microporous and mesoporous materials. Raman spectroscopy monitors the evolution of precursors and intermediates during synthesis under operational settings. Information on catalyst-reactant interaction and a detailed investigation of reaction mechanisms are provided by Raman spectroscopy.

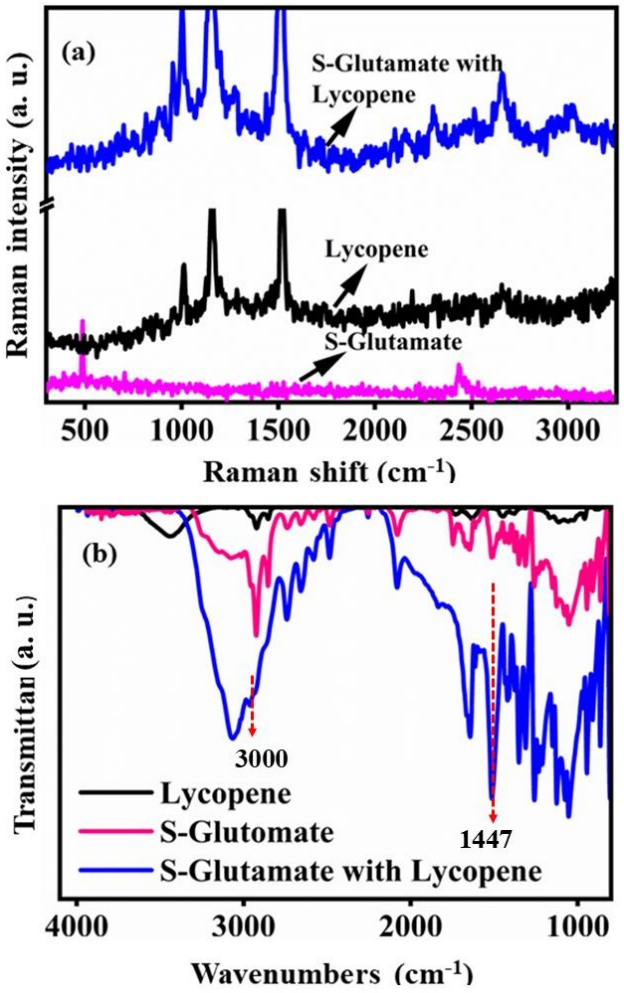

Figure 1. (a) Raman and (b) FTIR images of S-glutamate nanoparticles at the pyrolysis temperature 100 °C for the reaction time of 15 min (0.076 g glutamic are exposed to 0.22 L volume of H_2S gas in the presence of catalyst 0.6 mg lycopene.

After lycopene was added to S-glutamate, the "—SC-N–" species were identified by the Raman band at 2700 cm^{-1}, whereas the "SH–" species in the S-glutamate molecule were identified by the Raman band at 2450 cm^{-1}. Where there is no peak for the Locopene molecule in those frequency regions, it is attributed that the compound's electrons are transferred from glutamate to glutamide, according to Raman spectra, which may be the reason for the elevated catalytic activity.

In figure 1b, IR spectra were displayed in order to validate the functional groups in the S-glutamate particles that are both modified and unmodified with lycopene. As seen in the above figure, the large IR bond that corresponds to aromatic C-H bending in thiomide@lycopene appears at approximately 3000 cm^{-1}. Due to interaction with lycopene and water molecules, the CH•O band is redshifted, and its intensity is suppressed compared to that of unmodified thioamide. It is found that the number of peaks are observed at 3000 cm^{-1}, 2548 cm^{-1}, 1645 cm^{-1}, 1445 cm^{-1}, and 1080 cm^{-1} corresponds to the aromatic C-H bending vibration and the N-H, C-H (benzene ring), C-S, C-C, N-C (the C of benzene ring), -S-, and N-C (the C attached to S) [17–19]. The

difference between thiomides @ lycopene and individual aspartic thiomide molecules is observed over a wider range of wave numbers and vibrational frequencies. This is attributed to the increased interactions in hybrids. The bond at 1445 cm^{-1} is assigned to the sulfur methyl group (R-S-R + -CH_2-R).

It also noted that the peaks (figure 1) intensity changes upon modification could be a sign of modifications to the nanoparticles' electronic environment, conformational changes, or molecular interactions. A higher peak intensity, for example, might indicate a more advantageous interaction between lycopene and the S-glutamate framework, which could improve the stability or reactivity of the nanoparticles. On the other hand, a drop in intensity could indicate a structural rearrangement or a weakening of particular interactions that could impact the functionality of the nanoparticles by relating these spectral shifts to possible uses, like drug delivery or antioxidants, etc.

The surface composition of S-glutamate nanoparticles was studied by EDS. It has been discovered in figure 2 that the S-glutamate nanoparticles have four elements on their surface: carbon, nitrogen, oxygen, and sulfur. Their EDS peaks are 0.25 keV, 0.4 keV, 0.55 keV, and 2.5 keV, respectively. Additionally, it has been noted that the percentages of these four elements, carbon (100%), oxygen ($25-65\%$), nitrogen ($2-15\%$), and sulfur ($5-10\%$) over the glutamate particles. Following the use of lycopene, due to the lack of carbon species and partial elimination of unstable oxygen atoms during the reaction between glutamic acid and lycopene, the peak intensity for carbon remains constant while it varies for oxygen. According to the elemental mapping, the distribution of oxygen and sulfur species across the mesoporous hydrocarbon is expected to be homogenous, with a good degree of spatial overlap between carbon and nitrogen elements. It is possible that this unique arrangement of ordered mesoporous carbon surrounded by hydrogen atoms will facilitate electron transfer, prevent amino group leaching, and improve the catalytic stability and activity of the final product [20].

Figure 3 shows topographical pictures of S-glutamate nanoparticles prepared under different laboratory conditions. As shown in the first image, glutamate particles have a spherical shape, are intact, and range in size from 20 to 30 nm. Furthermore, lycopene appears to be a two-dimensional sheet with many naturally occurring nanopores on the interior surface that open the active sites and operate as a hollow shell that can be used as a template to physically absorb nearby H_2S and glutamic molecules.

In fact, these macro/micro channels served as a mass-transfer pathway that brought incident H_2S flux onto the inner surface of amino molecules in the lycopene layer, thus improving the catalytic process significantly. Thus, glutamate particles are produced and effectively confined as ultra nanoclusters in the lycopene layer via mesopores and microchannels. When a solvent, such as water or ethanol, is applied, it is found that the glutamate nanoparticles are agglomerated to be clustered and form enormous spherical domains. It is also noted that these particle clusters are not very cohesive.

Figure 4 shows the size distribution analysis used to calculate the mean size for glutamate and glutamate composites under laboratory conditions (catalyst, solvents, and reaction time). Using the Image J simulation, the average size of the glutamate particles- which are created either with the solvent involved in the reaction or without catalyst predicted to be between 1 and 10 nm. Additionally, the plots show that

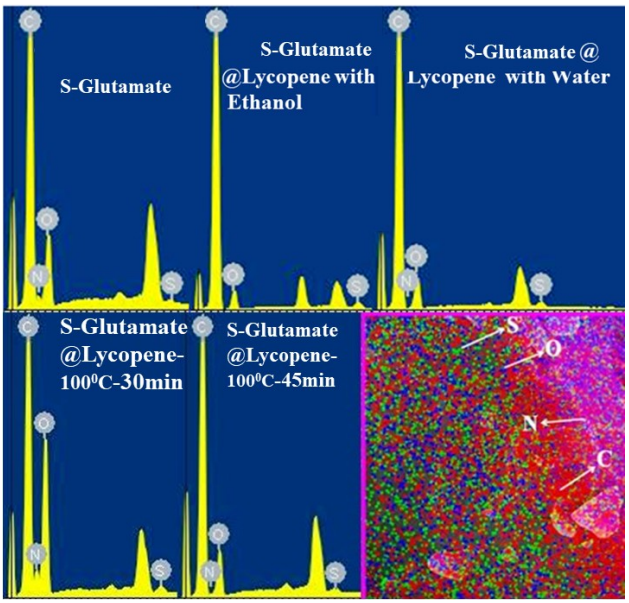

Figure 2. EDS images of S-glutamate nanoparticles and their elemental mapping at the temperature 100 °C for the reaction time of 15 min (0.076 g glutamic are exposed to 0.22 L volume of H_2S gas in the presence of catalyst 0.6 mg lycopene).

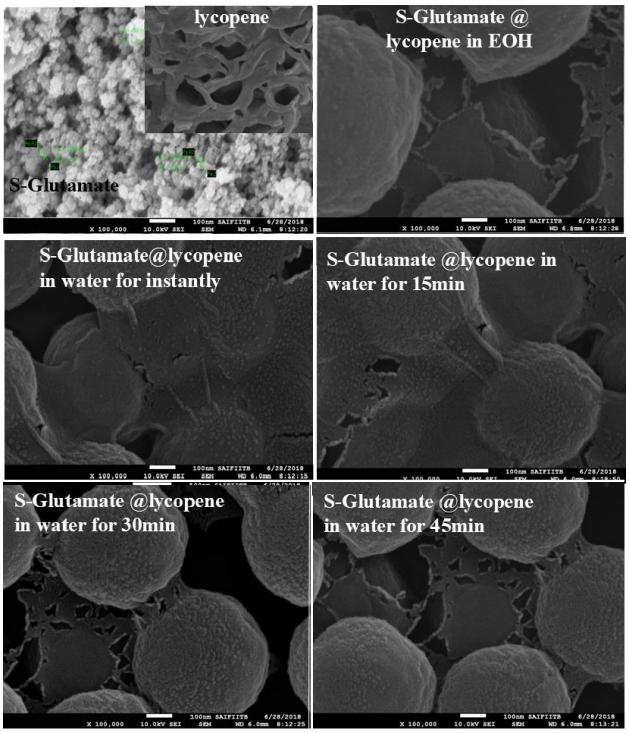

Figure 3. SEM images of S-glutamate nanoparticles for the various laboratory conditions (0.076 g glutamic are exposed to 0.22 L volume of H_2S gas for the various reaction times of 15 min, 30 min, 45 min in the presence of catalyst 0.6 mg lycopene).

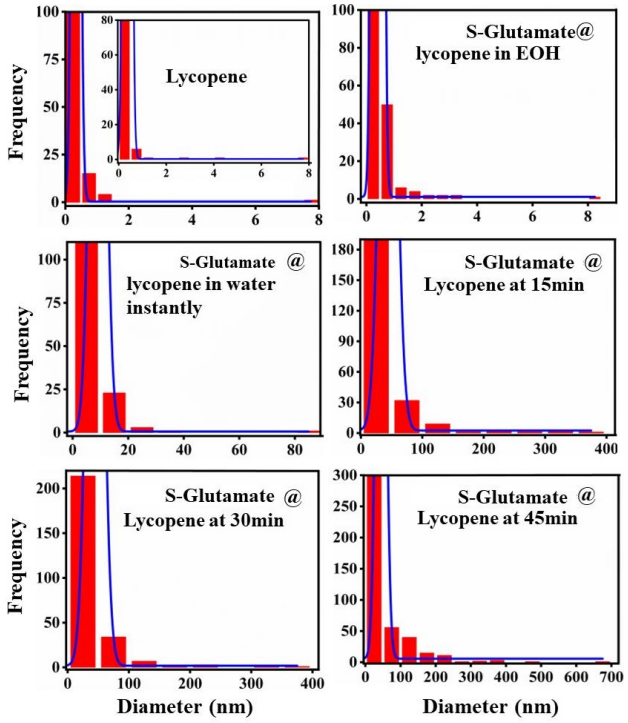

Figure 4. Size distribution images of S-glutamate products for the various laboratory conditions (0.076 g glutamic are exposed to 0.22 L volume of H_2S gas in the presence of catalyst 0.6 mg lycopene).

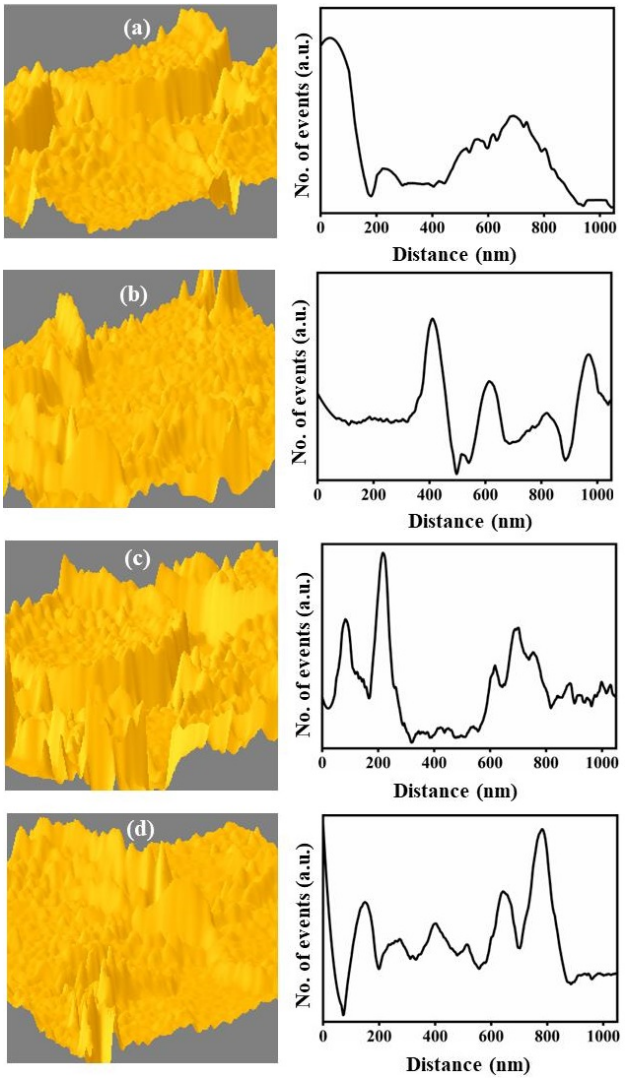

Figure 5. shows the roughness profiles corresponding to the various S-glutamate particles.

the glutamate particle size distribution varied differently with the various response periods; hence, it is presumed that the glutamate particle mean size automatically changed with the reaction time. It is approaching the range of 10 nm to 50 nm as the reaction time grew. Glutamic molecules are said to be evenly implanted across the lycopene layers' surface. The presence of mesopore-containing channels in lycopene can enhance particle harvesting and provide a large surface area for particle adsorption, leading to a significant rise in the mean size glutamate products.

Figure 5 depicts the surface roughness characterization of S-glutamate nanoparticles and values of various roughness parameters of glutamate nanoparticles are listed in Table 1. The average surface roughness Ra of S-glutamate nanoparticles was also calculated from these topographic histograms by using Image J software. It is defined as [21]:

$$R_a = \left(\frac{1}{N}\right)\sum_{i=1}^{N}|Z_i - Z_0| \qquad (1)$$

Here N is the number of sample points within the analyzed area from the mean line, and $|Z_i - Z_0|$ represents the absolute value of the profile deviation where Z_i is the current value and Z_0 is the average value within the analyzed area. One can note that average surface roughness R_a increases linearly with the full width at half maximum of topographic histograms.

The average surface roughness rises from 6.42 nm to 12.62 nm as reaction time increases. It was explained by the creation of tiny vacancy clusters inside the crystalline glutamate particle surface on the lycopene surface, which were caused by the aggregation of deformation-induced radical species such as H, $S^{\bullet}$, and $C^{\bullet}$ as well as the adsorption of H_2S molecules. The shapes of the heat-affected areas (figure 5) are non-symmetrical, affecting the regions on the

Table 1. shows the calculated roughness parameters of glutamate nanoparticles.

Reaction time (min)	R_{ms}	R_a	R_{sk}	R_{ku}	R_v	R_p	R_t	R_c	FPO	SA	R
0	8.17	6.42	0.73	1.06	-19.82	35.48	55.3	-0.5	59.8	3.81	0.23
15	11.45	8.13	0.92	1.72	-20.44	49.27	69.7	-0.1	59.9	3.83	0.30
30	13.64	9.75	0.94	1.77	-22.02	55.99	78.01	-0.0	60.1	4	0.50
45	16.92	12.62	1.13	3.29	-28.13	68.10	96.24	0.2	60.7	4.74	0.70

R_{ms} = root mean square roughness, R_a = Average roughness, R_{ku} = Kurtosis, R_{sk} = Skewness, R_v = Lowest valley, R_p = Maximum profile peak height, R_t = Maximum height of the profile, R_c = Mean Height, FPO = Mean polar facet orientation, SA = Surface area, R = Regularity ratio.

surface of molecules as compared to the surrounding regions due to non-uniform energy deposition. This increases the likelihood that lycopene particles will react with glutamate nanoparticles because the increase in surface roughness distributes the heat energy to a larger distance over the lycopene layer, causing holes or cavities to grow on the compound's surface [22].

Depending on the reaction type and duration, the catalyst's surface might be either rough or smooth. A rough surface has many tiny peaks and valleys, so a catalyst has active sites - the atoms or crystal faces where the reaction really takes place. With surface roughness, the reaction's rate rises and its overall activation energy decreases. It indicates a greater surface area. Therefore, using a powdered catalyst will increase the catalyst's surface area, ensuring that there are more collisions on the catalyst itself and a faster rate of reaction. Therefore, high conversion efficiency is obtained. As evidenced by the dips in figure 5(a)-(d), energy is deposited more unevenly in some locations than in other nearby regions. The hydrodynamic flow of H_2S species may be the cause of these affected regions, which leads to the creation of ridges and dips on the surface. Once a small dip forms, the heat beam's repeated reflections off the walls of the dip boost heat absorption, resulting in a smooth surface. The depth of the dips, which are caused by exfoliation colliding, also shows the solid flakes. The latter is a polar facet orientation-like mechanism that causes H_2S to separate from the lycopene surface as solid flakes as a result of recurrent thermal shocks, kurtosis, and material skewness [23].

The hydrogen sulfide solution on the porous surface during this reaction time causes the molten material to move outward from the center of the impact site and assigns the temperature gradient to the lycopene surface. As a result, a liquid tends to be pulled away from the surface region toward the deeper region of the molten surface heated by lycopene heat. This results in variations in polar orientation, peak height, and length evaluation (distance between the highest and lowest points of a particular peak) on the surface of lycopene particles, as illustrated in figure 5(a)-(d).

To elucidate the glutamate particle structure even more, figure 6(a-d) displays the results of a two-dimensional fast Fourier transform analysis conducted using scanning electron microscopy images to examine the configuration of active sites on the surface of glutamate nanoparticles. Thus, using the radial averages functions as the distance distribution between interaction sites and reaction time.

It is evident that a longer reaction time results in a more intense effect and a smaller radial average maximum peak, which decreases the interactive sites' distance distribution and increases the number of active sites on the glutamate particles' surface. In contrast, the less response time, the less intense the effect, the more distinct and larger the FFT radial average, the wider the distribution of the distance between active sites, and the fewer active sites generated on the surface of glutamate are all associated with shorter reaction times [24].

The radial average is displayed in figure 6(b), which was helpful in determining the regularity ratio (R) of glutamate

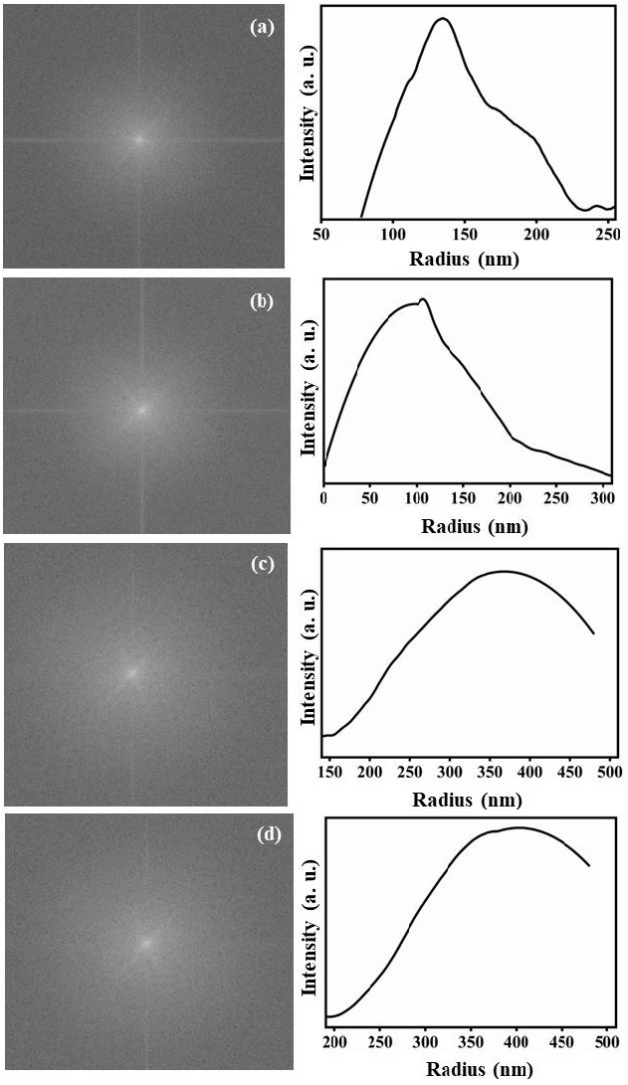

Figure 6. shows correction of abnormal intensity distribution of glutamate particles on fast Fourier transform pattern extracted from SEM image by using Image J.

particles using the formula

$$R = \frac{I}{W} \tag{2}$$

where I stand for intensity, W for full width at half of the intensity, and R for regularity ratio [25].

The regularity ratio on the surface of glutamate particles was found to be much greater in the case of large reaction time by longer sulfurization, because it was found that interactive sites distance reduces with increase in reaction time.

The zeta potential is related to the electrophoretic mobility by the Henry equation shown below, where η is the viscosity of the dispersant, U_e is the electrophoretic mobility, z is the zeta potential, ε is the dielectric constant, and $f(k_a)$ is the Henry function [26].

$$Subscript \qquad U_e = \frac{2\varepsilon z f(k_a)}{3\eta} \tag{3}$$

Figure 7 depicts Zeta potential; it provides information about the colloidal system's stability. As following the

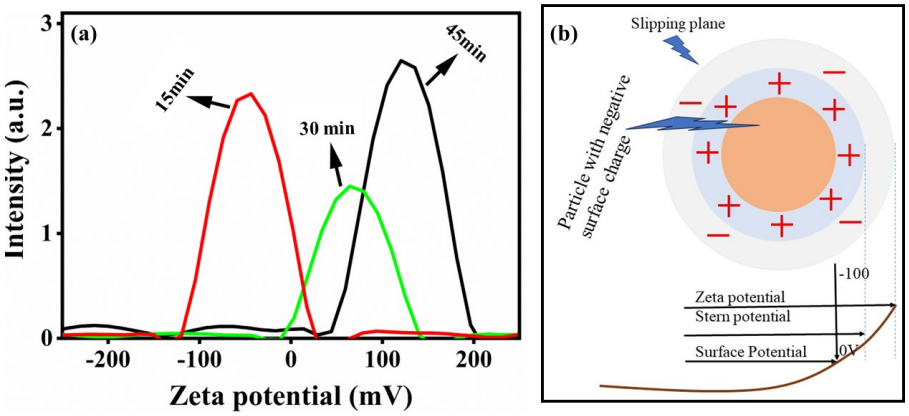

Figure 7. shows a typical plot of the zeta potential of glutamate particles versus reaction time (0.5 g NaCl, 10 mL water, 10 min sonicated time, 0.025 g glutamic thiomide nanoparticles).

method described above, all the particles in the suspension have a large negative or positive zeta potential; there could be no tendency for particles to come together. Particles will, however, clump together and flocculate if their zeta potential is low. Particles are considered unstable when their zeta potential falls between +30 mV and -30 mV. Zeta potentials of stable particles are typically larger than +30 mV or lower than -30 mV. But if the density of particles is higher than that of the dispersion. Thus, it is evident that the zeta potential is dependent upon both the surface and the type of dispersant.

The plot shows zeta potential against the reaction time, which will be positive at longer reaction times and negative at shorter reaction times. Using the zeta potential as a guide, the plot was used to predict that particles prepared at a long reaction time would be more stable, whereas particles prepared at a short reaction time would be less stable. The stability of nanoparticles is inferred by the increased zeta potential, which is caused by an increase in the amount of charged ions with opposite polarity over the surface of the glutamate particle. This increases the electrostatic interaction between the particles and their high surface energy. Reduced stability results from smaller response times, fewer ions covering the particle surface, smaller potential values, and uneven distribution of electric charges on the particle surface due to higher electrostatic repulsion [27].

As reaction time between the ions glutamide particle increases, increase their surface energy, hence increase the electrostatic interaction among the particles, which inturn amount of charged ions with opposite polarity over the thiomide particle surface increases, leading to the enhansion of zeta potential. The catalytic performance would be enhanced by this potential increase in the tendency to flocculate the particles, improve ion adhesion over the particle surface, and increase the adsorption ability of the catalyst.

Particle density can also significantly affect the Zeta potential through several mechanisms: Higher particle density can influence the distribution of charge in a colloidal system. Denser particles may lead to increased proximity and interaction among particles, which can enhance attractive van der Waals forces and reduce the effective electrostatic repulsion, potentially lowering the Zeta potential. In concentrated suspensions, the electric double layer surrounding each particle can overlap, affecting the overall potential. When particle density increases, the interaction between the double layers can modify the Zeta potential, often leading to a decrease as particles come closer together. Higher-density particles might also change the local environment in the dispersion medium. This could alter the viscosity and ionic strength of the solution, which in turn affects the mobility of the particles and their Zeta potential. As particle density increases, the likelihood of aggregation can also rise. Aggregated particles may have different surface characteristics and charge distributions, resulting in altered Zeta potential readings compared to well-dispersed systems. The Zeta potential is directly related to the electrophoretic mobility of particles. Denser particles may exhibit different mobilities under an applied electric field, impacting the measured Zeta potential. Understanding these interactions is crucial for predicting the stability and behavior of colloidal systems.

The optical absorption spectra of the glutamate nanoparticles using UV-visible spectroscopy based on the laboratory conditions are shown in figure 8. The intensity of the max-

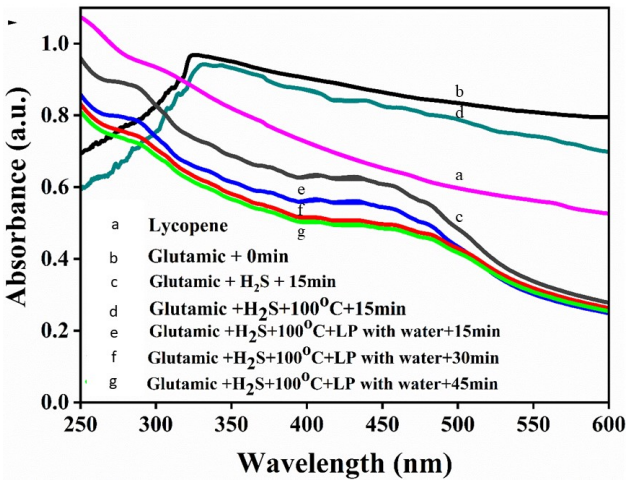

Figure 8. shows the change in absorbance spectra of S-glutamate for various laboratory conditions, revealing 58.9% conversion in the presence of thermal decomposition of lycopene and H_2S for 45 min, respectively. The concentration of the glutamic acid in the catalytic process experiment is 0.076 gr, and the dosage of the lycopene is 0.6 mg.

imum absorption peak of the glutamate particles reduced gradually with time and other factors. It can also be noted that the maximum wavelength of absorption was changed in the range of 321.5 nm - 290 nm after reaction durations of 15 min and 45 min, respectively. The shifting of the absorption wavelength with respect to the reaction time revealed the catalytic conversion of the glutamic acids. Eventually, the unique absorption peak became wide and weak in intensity, indicating the catalytic transformation of glutamic acids.

When lycopene with water was added to the glutamic article at 100 °C, the position of the maximum absorption band of the glutamine nanoparticle blue-shifted from the high-intensity wavelength of 332 nm to a lower intensity wavelength of 283 nm (figure 8(d-e)). As reaction time increased, the absorption band also changed from blue to red from 283 nm to 288 nm and 292 nm (figure 8(e-g)). Depending on the laboratory environment, different reactions to glutamide absorption occur. A red shift in the absorption spectra is caused by the mixing of lycopene and water in the glutamic clusters; when compared to undoped glutamic particles, the low wavelength region, in particular, displayed significant changes in the absorption behavior. The absorption spectra may redshift from the deep UV to the edge UV region as reaction time increases due to crystallite size. Red shift in the UV region would increase the absorption of light, which could be advantageous for photo-catalysts. The reason for this redshift could be a softening increase in the O-bond and S-band between the glutamic and lycopene particles, as opposed to the undoped glutamic thioamide, which has a slightly lower oxygen concentration because of the blue shift.

A number of factors may also be responsible for the observed shift in the absorption wavelength and weakening of the peak intensity in the UV-visible absorption spectra of glutamate nanoparticles during catalytic transformation. These may include 1) Changes in Particle Size and Shape: As the reaction progresses, the particle size and shape of the glutamate nanoparticles may change, leading to alterations in their optical properties. This, in turn, can cause a shift in the absorption wavelength and a decrease in peak intensity. 2) Surface Chemistry Modifications: The catalytic transformation may involve changes in the surface chemistry of the nanoparticles, such as the formation of new functional groups or the alteration of existing ones. These changes can affect the electronic transitions and, consequently, the absorption spectra. 3) Aggregation or Dispersion: The nanoparticles may undergo aggregation or dispersion during the reaction, influencing their optical properties and leading to changes in the absorption spectra. 4) Reaction Intermediate Formation: The formation of reaction intermediates or byproducts may also contribute to the observed changes in the absorption spectra.

The H_2S flux can significantly impact the catalytic activity of lycopene in the glutamic acid conversion reaction. It is noted from the above figure that when no temperature or H_2S is added, no glutamic acid transformation would occur. When using H_2S as the sulfur source, temperature involvement shows a distinct difference in activity. For instance, H_2S at room temperature gives only 19.9% glutamic conversion and 22.56% glutamate selectivity. As the temperature is applied, glutamic acid conversion increases evidently for H_2S at a temperature of 100 °C, which yields 27.3% conversion along with 29.1% glutamate selectivity. The interaction between H_2S and the catalytic sites can be influenced by several factors. For example, the binding modes of H_2S to the catalytic sites can affect the reaction kinetics and conversion efficiency. Different binding modes, such as σ-donation or π-back bonding, can influence the electronic properties of the catalyst and the reactants. Another example is the concentration of H_2S in the reaction mixture can influence the reaction kinetics and conversion efficiency. High H_2S concentrations can lead to an increase in reaction rate but may also result in the formation of unwanted byproducts.

In the glutamic acid catalytic method, we also included two more control variables, such as catalyst and reaction time. One is lycopene, which acted as a catalyst under the same conditions and performed better in the glutamic acid conversion, suggesting that its mesoporous shape helps the substrate reach the active sites and increase catalytic activity. Lycopene-ethanol, when used as a solvent, yields a glutamic acid conversion of just 28.68%, suggesting that ethanol activates lycopene less effectively and dissociates more quickly than molecular H_2S to provide adsorbed sulfur atoms needed for the sulfurization of glutamic acid. Subsequently, we examined how the presence of water as a solvent affected the reaction rate. For example, 59.6% glutamic conversion and 64.2% glutamate selectivity are obtained when lycopene and water are combined. Water is a cheap, environmentally benign green solvent. Both the simple diffusion impact of organic molecules in hierarchically porous structures and the activity of macro channels as mass transport paths for injecting H_2S flux onto the inner surface of amino molecules can be linked to the increase of selectivity. Reaction time is another important factor for the catalytic reaction [28, 29], while the H_2S flow rate, reaction temperatures, and reagent concentrations remain almost constant. As the reaction period increases from 15 to 45 min, there is a noticeable increase in glutamic acid conversion for lycopene water, with a conversion rate of 71.9% and glutamate selectivity of 89.2%.

To assess the encapsulation effect by assessing the crystalline characteristics, XRD measurements (figure 9) were made directly on the surface of catalyzed products. Glutamic acid molecules are represented by the typical peaks at 23.7° and 20.5°, respectively. Additionally, the composites with 2θ values at 23.6°, 25.5°, 26.1°, 27.0°, 28.1°, and 31.2° showed the crystalline form of sulfur (S8), which may be related to the reaction of S_2^- and SCO_2^- in the catalytic sulfurization process that was observed of sulfur atoms in glutamate. As stated in references [30, 31], the amino groups were seen to exhibit peaks at 2θ values in the range of $35-40°$ (JCPDS No: $30-1740$,$32-1701$). Glutamate is confirmed to belong to the orthorhombic crystal structure with space group P212121 and point group 222 based on the X-ray diffraction pattern [32]. The XRD spectra of glutamate at various reaction times are displayed in figure 9.

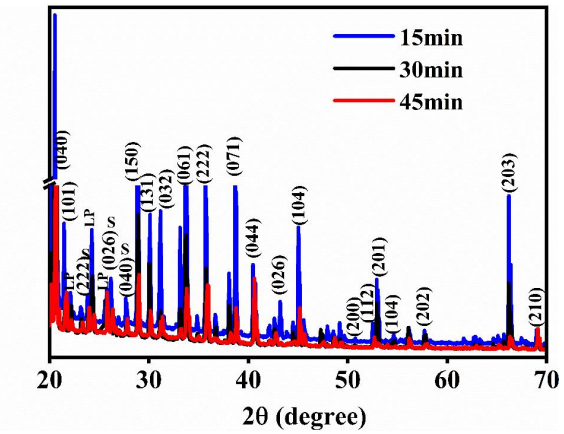

Figure 9. XRD spectra of S-Glutamate@lycopene at the temperature of 100°C for the various reaction times (0.076 g glutamic acid, 0.22 L volume of H_2S gas, and 0.6 mg lycopene).

When the heating duration is increased from 15 min to 45 min, the reflections progressively shift to higher 2θ values. All of the diffraction peaks show fewer significant changes in peak locations and intensities as the heating period increases from 30 to 45 minutes, suggesting that the structural order of glutamate has reached saturation. The diffraction peaks at 22°-26° were visible, indicating that lycopene was fully entrenched in the mixture of lycopene and glutamate [33].

X-ray diffraction is used to examine the crystal structure of glutamide nanoparticles with reaction time. The X-ray diffraction of glutamide nanoparticles is shown in figure 8. Using the diffraction peak (040) at an angle of 20°, the crystallite size of the glutamide particle has been estimated using Scherrer's equation [32]. $D = K\lambda/\beta\cos\theta$ where D is the mean size of crystallite (nm), K is the shape factor equal to around 0.9, λ is the X-ray wavelength, 0.154 nm of Cu $K\alpha$ radiation, β is the line widening at half intensity of the peak (degrees), and $theta$ is the angle of the diffraction peak (degrees).

With reaction times of 15, 30, and 45 minutes, the glutamide particle's crystallite size was measured to be 10.3 nm, 19.9 nm, and 33.7 nm. It is evident that as reaction time increases, the average crystallite size of glutamide nanoparticles increases as well.

The XRD data of S-Glutamate@lycopene at 100 °C for various reaction times reveals changes in crystallinity, which can be attributed to structural transformations occurring during the reaction. A more detailed interpretation of the shift in 2θ values and its correlation to structural transformations can provide valuable insights into the reaction mechanism. Crystallinity refers to the degree of structural order in a solid. Higher crystallinity often results in a more stable and less reactive material, which can slow down the reaction kinetics. In the context of glutamic acid, a lower crystallinity may lead to increased surface area and more active sites, facilitating faster reaction rates. As crystalline decreases, the material becomes more amorphous, which can enhance the solubility and reactivity of glutamic acid. This may lead to improved conversion efficiency to S-Glutamate@lycopene, as the reactant is more readily accessible for reaction.

Conclusion

In this work, we have synthesized the S-glutamate nanoparticles using the reagents of glutamic acid and hydrogen sulfide molecules via a catalytic sulfurization process. The catalytic sulfurization process is a simple, cost-effective, and environmentally friendly way. It involves heating hydrogen sulfide to a temperature of around 100 °C and extracting sulfur from it by attaching a carbon atom of a carboxylic group at the end of a glutamic acid carbon chain. Lycopene, a carotenoid, acts as a useful and effective catalyst to initiate the reaction between amino and gaseous molecules when heat energy is applied. The mean size of glutamate nanoparticles is estimated based on the size distribution using Image J analysis; it is found to be in the range of 10 nm to 50 nm. Here, the surface roughness characteristics that are influenced by reaction time towards the preparation of glutamate nanoparticles will have a more significant impact on the catalytic properties. Zeta potential increases from 40 to 115 because of increased electrostatic repulsive force between the particles, which is followed by an increase in adsorbed molecular concentration as reaction time increases. In the thermal breakdown of H_2S gas as the sulfurizing agent, the lycopene heated to 100 °C particles were found to exhibit extraordinary catalytic activity for sulfurizing glutamic acids, resulting in the formation of glutamate particles with 89% selectivity, respectively.

Acknowledgments

This work was supported by the Mahatma Gandhi Institute of Technology

Authors contributions

Martha Ramesh contributed to the preparation and characterization of samples and the writing of this article. A Santhosh Kumar and Ganji Saidulu contributed to the literature survey and analysis of results. Ravuri Venkateswara Rao and Ravoori Nagaraju contributed in plotting of figures and organization of this article. K. Chandrakanta and Alok Barik also contributed in the simulation of results through software (Image J) and reviewing this work. P. V. Chandrasekar and Arijit Mondal contributed in giving proper shaping and checking the similarity of this work.

Availability of data and materials

Data and materials should be accessible for a reasonable time after publication.

Conflict of interests

We are ensuring that the article remains free from competing interests.

References

[1] H. L. McLain, D. P. Glavin, J. P. Dworkin, E. T. Parker, J. E. Elsila, J. C. Aponte, D. N. Simkus, C. I. Pozarycki, H. V. Graham, L. R. Nittler, et al. *Meteorit. Planet. Sci.*, **55**(2020):1979. DOI: https://doi.org/10.1111/maps.13560.

[2] A. Yousefi and A. N. Ejhieh. *Iran. J. Catal.*, **11(3)**(2021):247–259. URL https://journals.iau.ir/article-684355.

[3] M. G. Chegini, M. Mokhtary, and A. Pourahmad. *Iran J. Catal.*, **14(2)**(2024):1–12. DOI: https://doi.org/10.57647/j.ijc.2024.1402.12.

[4] D. P. Glavin, J. E. Elsila, H. L. McLain, J. C. Aponte, E. T. Parker, J. P. Dworkin, D. H. Hill, H. C. Connolly, and D. S. Lauretta. *Meteorit. Planet. Sci.*, **56**(2021):148–173.
DOI: https://doi.org/10.1111/maps.13451.

[5] Koga T. and H. Naraoka. *ACS Earth Space Chem.*, **6**(2022):1311–1320.
DOI: https://doi.org/10.1021/acsearthspacechem.2c00008.

[6] Q. Zhang, L. Zhang, X. Cheng, and Z. Qi. *Iran J. Catal.*, **14(2)**(2024):1–12.
DOI: https://doi.org/10.57647/j.ijc.2024.1402.09.

[7] F. Pietrucci, J. C. Aponte, R. Starr, A. P. Villa, J. E. Elsila, J. P. Dworkin, and A. M. Saitta. *ACS Earth Space Chem.*, **2**(2018):588–598.
DOI: https://doi.org/10.1021/acsearthspacechem.8b00025.

[8] T. Magrino, F. Pietrucci, and A. M. Saitta. *Phys. Chem. Lett.*, **12**(2021):2630–2637.
DOI: https://doi.org/10.1021/acs.jpclett.1c00194.

[9] M. A. Matsko, Semikolenova N. V., and V. A. Zakharov. *Catal. Chem. Petrochem. Indust.*, **15**(2023):267–277.
DOI: https://doi.org/10.1134/S2070050423030066.

[10] L. N. Nasirmahale and F. Shirini. *Iran J. Catal.*, **14(2)**(2024):1–12.
DOI: https://doi.org/10.57647/j.ijc.2024.1402.17.

[11] J. G. Kim, S. J. Yoo, C. Y. Kim, and H. T. Jou. *Appl. Microscop.*, **44(4)**(2014):138–143.
DOI: https://doi.org/10.9729/AM.2014.44.4.138.

[12] S. Ghattavi and A. N. Ejhieh. *J. Mol. Liq.*, **322**(2021):114563.
DOI: https://doi.org/10.1016/j.molliq.2020.114563.

[13] McElroy M. B. and S. C. Wofsy. *Atmospheric Environment*, **14(2)**(1980):159–163.
DOI: https://doi.org/10.1016/0004-6981(80)90274-7.

[14] M. M. Huo, W. L. Liu, Z. R. Zheng, W. Zhang, Li A. H., and D. P. Xu. *Molecules*, **16**(2011):1973–1980.
DOI: https://doi.org/10.3390/molecules16031973.

[15] P. Bazylewski, R. Divigalpitiya, and G. Fanchini. *RSC Adv.*, **7**(2017):2964–2970.
DOI: https://doi.org/10.1039/C6RA25879D.

[16] A. L. Jenkins, Larsen R. A., and T. B. Williams. *Spectrochimica Acta Part A: Molecular and Biomolecular Spectroscopy*, **61(7)**(2005):1585–1594.
DOI: https://doi.org/10.1016/j.saa.2004.11.055.

[17] A. Owhal, A. D. Pingale, S. U. Belgamwar, and J. S. Rathore. *Alloys and Metallurgical Systems*, **6**(2024):100083.
DOI: https://doi.org/10.1016/j.jalmes.2024.100083.

[18] Z. Shirazi, A. N. Golikand, and M. H. Keshavarz. *Iranian Chemical Society*, **21**(2024):409–419.
DOI: https://doi.org/10.1007/s13738-023-02933-4.

[19] G. Liu, L. Liu, Y. Zhou, Y. Wang, Sui G., and P. Zhang. *Iranian Chemical Society*, **21**(2024):877–885.
DOI: https://doi.org/10.1007/s13738-024-02968-1.

[20] Z. Wei, Y. Chen, J. Wang, D. Su, M. Tang, Mao S., and Y. Wang. *ACS Catal.*, **6**(2016):5816–5822.
DOI: https://doi.org/10.1021/acscatal.6b01240.

[21] I. Horcas, R. Fernández, J. M. G. Rodríguez, J. Colchero, J. G. Herrero, and A. M. Baro. *Review of Scientific Instruments*, **78**(2007):013705.
DOI: https://doi.org/10.1063/1.2432410.

[22] C. C. Harper, J. S. Jordan, S. Papanu, and E. R. Williams. *ACS Nano*, **18(27)**(2024):17806–17814.
DOI: https://doi.org/10.1021/acsnano.4c03503.

[23] C. Pfeiffer, C. Rehbock, D. Hu'hn, C. C. Carrion, D. J. de Aberasturi, V. Merk, Barcikowski S., and W. J. Parak. *J. R. Soc. Interface*, **11**(2013):0931.
DOI: https://doi.org/10.1093/ndt/gfs439.

[24] B. Wang, G. Fang, K. Tan, J. Liang, J. Ge, and S. Liu. *Composite Structures*, **247**(2020):112448.
DOI: https://doi.org/10.1016/j.compstruct.2020.112448.

[25] M. Ramesh and H. S. Nagaraja. *Mater. Today Chem.*, **3**(2017):10–14.
DOI: https://doi.org/10.1016/j.mtchem.2016.12.002.

[26] M. Kaszuba, J. Corbett, F. M. Watson, and A. Jones. *Philos Trans A Math Phys Eng Sci.*, **368**(2010):4439–4451.
DOI: https://doi.org/10.1098/rsta.2010.0175.

[27] C. P. Romero, R. I. Jeldres, G. R. Quezada, Concha F., and P. G. Toledo. *Colloids and Surfaces A: Physicochemical and Engineering Aspects*, **538**(2018):210–218.
DOI: https://doi.org/10.1016/j.colsurfa.2017.10.080.

[28] F. Chen, C. Kreyenschulte, J. Radnik, H. Lund, A. E. Surkus, Junge K., and M. Beller. *ACS Catal.*, **7**(2017):1526–1532.
DOI: https://doi.org/10.1021/acscatal.6b03140.

[29] M. Uddin, Chowdhury S. E., and S. Elahi. *Water Conserv Sci Eng.*, **7**(2022):351–361.
DOI: https://doi.org/10.1007/s41101-022-00146-z.

[30] H. Li, Q. Z. Yao, Y. Y. Wang, Li Y. L., and G. T. Zhou. *Scientific Reports*, **5**(2015):7718.
DOI: https://doi.org/10.1038/srep07718.

[31] L. Yao, X. Min, H. Xu, Y. Ke, Y. Liang, and K. Yang. *Int. J. Environ. Res. Public Health*, **15(9)**(2018):1863.
DOI: https://doi.org/10.3390/ijerph15091863.

[32] P. Dhanasekaran and K. Srinivasan. *Cryst. Res. Technol.*, **47(12)**(2012):1217–1230.
DOI: https://doi.org/10.1002/crat.201200053.

[33] J. Uma and V. Rajendran. *Progress in Natural Science: Materials International*, **26(1)**(2016):24–31.
DOI: https://doi.org/10.1016/j.pnsc.2016.01.013.